A CAD-Based Tool for Calculating Power Deposition on Tokamak Plasma-Facing Components

Wayne Arter, *Member, IEEE*, Valeria Riccardo, and Geoff Fishpool

***Abstract*—The SMARDDA software library is used to model plasma interaction with complex engineered surfaces. A simple flux-tube model of power deposition necessitates the following of magnetic fieldlines until they intersect the geometry taken from a computer aided design (CAD) database. Application is made to: 1) models of ITER tokamak limiter geometry and 2) MAST-U tokamak divertor designs, illustrating the accuracy and effectiveness of SMARDDA, even in the presence of significant nonaxisymmetric ripple field. SMARDDA's ability to exchange data with CAD databases and its speed of execution also gives it the potential for use directly in the design of tokamak plasma-facing components.**

***Index Terms*—Fusion reactor design, plasma transport processes, thermal management, tokamaks.**

I. Introduction

The problem of economic electrical power generation using tokamak nuclear fusion continues to generate new technological challenges, even as the basic issues involved in magnetically confining plasma become better understood. Tokamak reactor designs anticipate long periods, months to years in length, of continuous plasma discharge operation at powers of up to 2 GW. Helium ash produced by fusion that could otherwise prematurely terminate a discharge must be continually removed from the edge, most likely taking with it a significant fraction of the total plasma power. Even in large tokamak experiments, the deposition of plasma energy lost from the edge onto likely construction materials has the potential to do serious structural damage if restricted to a relatively small areas of the size of the plasma scrape-off layer with its 1 cm or so thickness.

Plasma-facing component (PFC) is a generic term for any part of the tokamak apparatus, which could conceivably suffer a significant amount of power deposition. The main types are limiters that are at least in part touching the plasma edge (see Fig. 6 in Section III for illustration), and divertors, into which escaping plasma is channeled to be cooled and/or spread out (see Fig. 11 in Section IV) and which are expected to be an essential component of a power-producing reactor. In either case, the physical objects interacting with plasma consist of panels or tiles made of or at least coated with refractory metal, protecting complex structures that, for example, provide active cooling. Although greater interest attaches to power handling in divertors, most scenarios for tokamak discharge start-up involve a period of limiter operation with a comparatively energetic plasma.

This paper shows how a relatively small development of the software algorithms and modules described for a neutral beam application in companion Paper I [1] has allowed the SMARDDA code to examine power deposition in both limiter and divertor geometries. The limiter studies were in support of ITER [2], whereas divertor designs were tested for the upgrade of the MAST spherical tokamak at Culham [3]. Although in both cases, SMARDDA was used to verify engineering designs produced by others, the speed of execution of the software would enable it to be more directly involved the design process.

A. Power Deposition Problem

Since the edge plasma is relatively cool, indicative temperature 10 eV, yet the field is relatively high, indicative level 5 T (in ITER), the typical ion gyroradius is very small, 100 μm compared with a plasma minor radius measured in meters. Hence, as a consequence of the individual motions of the charged particles (ignoring turbulent collective effects), the plasma that interacts with PFCs simply flows along the lines of magnetic field. To spread the power over as large an area as possible, it is therefore best to arrange the PFCs so that magnetic fieldlines are at close to tangential incidence on their surfaces, see formula for power deposition Q in Section II-B.

For a given field alignment and shallow angle of incidence, designing individual tile surfaces is relatively straightforward [4]. However, this is not a complete answer, in that first the fieldlines are not strictly straight and second, the actual installation may differ substantially from the ideal, notably through the presence of gaps, and installation tolerances will allow minor misalignments. The gaps, where power might flow between the tiles/panels, are necessary to give clearances for installation and to allow for thermal expansion during discharges. Since the edges of the tiles, i.e., those

Manuscript received February 20, 2014; revised March 31, 2014; accepted April 22, 2014. Date of current version July 8, 2014. This work was supported in part by F4E under Contract F4E-OPE-148, in part by the RCUK Energy Programme under Grant EP/I501045, and in part by the European Communities under the Contract of Association between EURATOM and Culham Centre for Fusion Energy.

This paper has supplementary downloadable multimedia material available at http://ieeexplore.ieee.org provided by the authors. This material is 0.15 MB in size.

The authors are with the Culham Centre for Fusion Energy, United Kingdom Atomic Energy Authority, Abingdon OX14 3DB, U.K. (e-mail: wayne.arter@ieee.org; valeria.riccardo@ccfe.ac.uk; geoff.fishpool@ccfe.ac.uk).

Color versions of one or more of the figures in this paper are available online at http://ieeexplore.ieee.org.

Digital Object Identifier 10.1109/TPS.2014.2320904

surfaces adjacent to the designed surfaces, are at nearly normal incidence to the field, they might have very high levels of power deposition unless nearby tiles were arranged to shadow them. However, it is also important to minimize the shadowing of one designed surface by another as shadowing increases the overall average power density.

Furthermore, particularly within a divertor geometry, it may be necessary to allow for fieldline curvature and ripple, whereas for limiters, it may be necessary to treat a range of different field alignments, corresponding to different types of discharges and different times within a discharge. Hence, there is the need for software, which can examine detailed designs of sets of tiles, ultimately defined using a computer aided design (CAD) system, and their interaction with an accurate 3-D representation of the magnetic field.

B. SMARDDA

As described in the companion Paper I [1], the SMARDDA software was developed to have in principle all of the features necessary to perform design-relevant calculations for PFCs. Ancillary software takes geometry modeled using the CATIA design system and converts it to the open vtk format [5] expected by the main modules, which describes the geometry as triangulated surfaces. Charged particles, produced by charge exchange reactions between a neutral beam and plasma in a duct, are tracked in a magnetic field until they strike the duct walls, and the resulting power deposition is examined. SMARDDA uses a specially designed algorithm involving a special multioctree type of hierarchical data structure (HDS) to speed particle tracking.

However, it is very inefficient to track particle motions directly when they anyway closely follow magnetic fieldlines, so development was necessary to solve the streamline or fieldline equation of motion. In addition, new formula for power deposition are required when it is the local magnetic flux tube that is responsible for the process, and new ways are needed to introduce particles into the model to represent the fieldlines.

Fortunately, the original SMARDDA development benefitted from the use of object-oriented Fortran in its implementation, which mandates the use of strictly defined and protected objects, hence a modular structure of code. The concept thus naturally developed that SMARDDA should become much more a library of object-oriented modules from which codes for specific purposes could be built as necessary. The original HDSGEN software written to generate the HDS needed for SMARDDA ray-tracing exemplifies such a code.

Many codes have been written to track streamlines of fluid flow, and indeed the facility is available in the freely available ParaView software [6] used for the visualization of vtk files and indeed for much SMARDDA output. However, the requirement for streamlines to intersect surfaces is more unusual, and to meet this only literature involving magnetic fields seems to be relevant. Particle-in-cell codes were discussed in Paper I, and as for codes designed specifically to follow fieldlines, most are either not interested in wall interactions or model them with idealized geometry. The only documented code with the capability to treat realistic CAD designs at the time of the SMARDDA development was Tokaflu [7], but this has a number of deficiencies, notably in respect of computational efficiency. The authors of the general-purpose ISDEP particle tracking software [8] do not explain how it treats complex geometry. Very recently a module has been added to the magnetic field equilibrium software CREATE to track fieldlines over triangulated geometry [9].

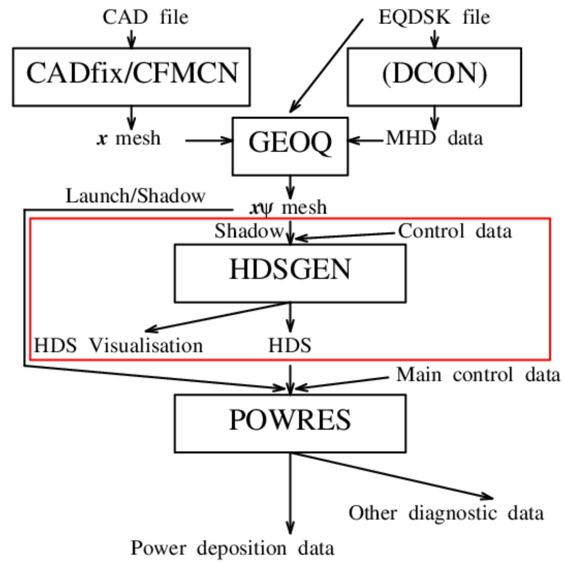

Fig. 1. Flow of data through the SMARDDA modules for limiter problems.

The new developments are discussed in the context of the use of SMARDDA to perform the different modeling tasks, see Section II-A.

II. General Methods of Calculation

A. Introduction

For both limiter and divertor cases, the geometry is logically divided into two types, the first is the part for which power deposition is to be calculated (the results geometry) and the second type is the geometry, which protects the edges of the first by fieldline shadowing (the shadowing geometry). An important practical point is where to start the fieldlines, and for efficiency it seems best to adopt the adjoint concept from computer graphics, namely to begin the fieldlines on the results geometry, and test whether they can be followed to the nominal source of power at the tokamak midplane without striking the shadowing geometry. Hence, the results geometry may also be referred to as the launch geometry, contrast Paper I where particles are launched to sample analytically defined beamlets and power is deposited on the shadowing geometry.

Fig. 1 shows the flow of data needed to calculate power deposition on limiter tiles/panels (the data-flow for the divertor case is very similar). The import of CAD (top left) using the CADfix package supplied by ITI TranscenData is discussed in detail in Paper I. Locally written software converts a CADfix mesh for either results or shadowing geometry into vtk format at the point labeled **x** mesh in Fig. 1, see Section II-C below for more details. EQDSK file (top right) denotes a file format, which describes a tokamak magnetic field equilibrium.

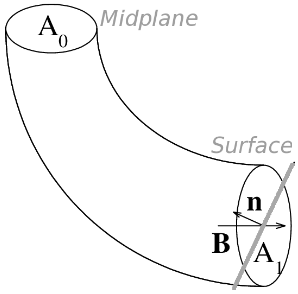

Fig. 2. Flux tube of field **B** connecting the torus midplane with a surface indicated schematically in gray with normal **n**. The flux tube area is A_1 at bottom right, at top left it is cut by a horizontal circle with area A_0.

Glasser's DCON code [10] may optionally be used to check the contents of the EQDSK file, or act as an interface to other equilibrium field file formats. The magnetic field **B** is assumed to be axisymmetric, independent of toroidal angle ϕ, and thus can be described by a (poloidal) flux function ψ, together with a toroidal component specified by the flux function $I(\psi)$.

In the limiter case, fieldline calculation takes place in a coordinate frame aligned with contours of ψ. Geometry and equilibrium data are combined by the GEOQ code to give the $\mathbf{x}\psi$ mesh file, which has the geometrical information in flux coordinates, see Section II-D below. The HDSGEN code, described in Paper I is shown in the red box to indicate that it is only required for processing the shadowing geometry. Although it is apparently, thereby implicitly assumed that the results geometry cannot be struck by a fieldline, the same tile triangulation can in fact be a part of both launch and shadowing geometry.

The fieldline tracing and power deposition calculations are then performed by the POWRES code, or the POWCAL code in the case of divertor calculations. The latter follows fieldlines using cylindrical polar coordinates in physical space. Features common to both codes are described in the remainder of this section, starting with the power deposition model as this informs subsequent material, which is ordered after the flow of Fig. 1. Model features and files specific to the treatment of nonaxisymmetric ripple field are described in Section IV.

B. Model of Power Deposition

A simple model of power deposition by plasma in flux tubes is used in calculations of the tokamak edge. Since it does not seem to have been fully documented elsewhere, details of the derivation of the principal formula are presented in the Support Section I. The basic idea may be explained using Fig. 2, which shows a flux-tube connecting the tokamak midplane with a physical surface of area A_1. As it is assumed that particles follow fieldlines, all power entering the top of the tube strikes the surface at bottom. Furthermore, the power at the top of the tube is assumed to fall-off exponentially with (major) radial distance at an empirically determined rate λ_m from the last closed flux surface (LCFS) [11]. The LCFS is given by $\psi = \psi_m$, where ψ_m is the value of the poloidal flux where the geometry touches the plasma, or equal to ψ at the X-point in case of divertor plasmas. In Support Section I, the power density Q deposited on the PFC is shown to vary as

$$Q = C_{\text{std}}\mathbf{B}\cdot\mathbf{n}\exp\left(-\frac{(\psi-\psi_m)}{\lambda_m R_m B_{pm}}\right) \quad (1)$$

where ψ is the flux function value for the tube at the midplane, and the other quantities including the power normalization factor C_{std} (Support Section I) are fixed for a given equilibrium and geometry. The formula is found to be a very accurate fit to data from many different tokamak experiments [12].

1) Eich formula for Power Deposition: Eich's formula [13] is relevant only to divertor geometries. It accounts for the spread of power into the private flux region of the divertor, apparently caused by some kind of collective plasma behavior. Relative to (1), there is an additional parameter σ to describe the fall-off length for power deposited in the private flux region, so that Q varies smoothly across the surface $\psi = \psi_m$, as

$$Q_E = C_E\mathbf{B}\cdot\mathbf{n}\exp\left[\left(\frac{\sigma}{2\lambda_q}\right)^2 - \frac{\Delta\psi}{R_m B_{pm}\lambda_q}\right] F_E(\psi) \quad (2)$$

where

$$F_E(\psi) = \operatorname{erfc}\left(\frac{\sigma}{2\lambda_q} - \frac{\Delta\psi}{R_m B_{pm}\sigma}\right) \quad (3)$$

and

$$C_E = \frac{F P_{\text{loss}}}{4\pi R_m \lambda_q B_{pm}}. \quad (4)$$

In the above, $\Delta\psi = \psi - \psi_m$, λ_q now denotes the characteristic decay length outside the private flux region, and other quantities are as defined in Support Section I. Despite its formidable appearance $Q_E(\psi)$ is analytically integrable and the normalization is exact.

C. Meshing and Mesh Refinement

1) Meshing: It is generally sufficient for limiter plasmas to consider shadowing by adjacent panels only, as confirmed by SMARDDA calculations with the ITER geometry, see Section III. This is not necessarily true for divertor plasmas, but for the MAST-U work there is the simplification that the divertor design has twelvefold symmetry about the major axis. Hence, in both cases, the region to be meshed is reduced to a small fraction of the total limiter/divertor area, since there are some 360 panels in ITER designs (compare over 100 tiles in MAST-U divertor).

A major saving both in user and computer time is achieved by only meshing the surfaces of PFCs. For MAST-U, compared with the typical tile or panel surface dimensions of 30 cm × 1 m, the intertile gaps are approximately 2 mm. This implies that to verify the absence of power deposition on the tile edges, triangles with a side of order this length will be required. A uniform meshing at 2 mm is excessive in requiring over 10^5 triangles per tile, so it is economical to produce a surface mesh, which grades down to this size only in the critical areas, as elsewhere a 30 mm spacing is sufficient, at least for exploratory calculations, see Sections III and IV.

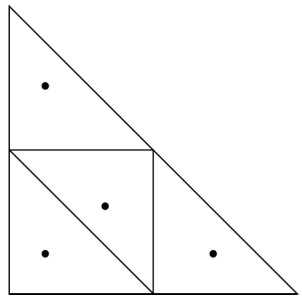

Fig. 3. Subdivision of a triangle into four congruent parts by geometry-conforming points, which is performed automatically by the CFMCN code.

2) Automatic Mesh Refinement: One unique feature of the CADfix package used for the meshing is its FORTRAN application programmer interface (API). This API has been used in the development of the CFMCN code capable not only of generating the vtk files describing triangulations, but also to produce a succession of refinements automatically for a given triangulation. Each triangle is separately divided into four congruent parts as shown in Fig. 3 with the important feature that the splitting points are geometry-conforming, i.e., they lie on the CAD surface and are not just averages of preexisting points. This ability to produce meshes at $\times 4$ and $\times 16$ resolution is most helpful for convergence studies.

3) Surface Accuracy: For the most part, it is the shadowing of PFC surfaces, which is the main issue. However, since power deposition $Q \propto \mathbf{B} \cdot \mathbf{n}$ with $\mathbf{B}$ arranged to be nearly perpendicular to $\mathbf{n}$, if accurate numerical values are needed, it is necessary to be able to reproduce the surface normal direction accurately. The economical approach to data adopted by SMARDDA relies on approximating the tile normal using the normals of the triangular facetting, rather than say augmenting the triangulation file with $\mathbf{n}$ values extracted from the CAD database. The consequent error in $B_n = \mathbf{B} \cdot \mathbf{n}$ is examined in detail in Support Section II for a simple configuration of a toroidal field (TF) intersecting a vertical cone of apex angle $\pi/2 - \alpha$.

Assuming that beyond a certain major radius, the cone is meshed with Union Jacks as explained in Support Section II, then the surface normal computed using plane triangular facets of toroidal angular extent $\Delta\phi$ has a component in the toroidal direction equal to $(\Delta\phi/2)\sin\alpha$. The factor of 1/2 arises ultimately because two edges define the normal. However, the logical place to calculate B_n is at the triangle barycenter where the geometry-conforming normal is found to contain a factor of 1/3, leading to an error in Q scaling as $\Delta Q \propto (\Delta\phi/6)\sin\alpha$. The Union Jack mesh, although pleasing to the eye, is actually here very bad for ΔQ. Even so, the linear scaling of error with mesh-spacing is likely to apply for most styles of triangulation, and accounts for the irregular appearance of Q plots on the (coarse) base meshes observed in later sections.

D. Magnetic Field Import

For input to GEOQ (Fig. 1), different ITER field distributions are specified using EQDSK files produced by the CREATE-NL software from the Consortio CREATE [14], whereas equivalent files for MAST-U work are produced by the locally written Fiesta code [15]. The file format specifies ψ as a set of values on a regularly spaced grid in (R, Z). Direct product cubic spline interpolation of the sample values and their derivatives using the de Boor package [16] is used in the obvious way to define the magnetic field at any point in the gridded region.

Once the flux has been interpolated, it is straightforward to calculate ψ_m for the limiter plasmas. To determine other parameters such as R_m and ψ_m for X-point plasmas, it is helpful to work in the coordinate system given by ψ and θ, poloidal angle measured about the O-point in the center $(R_{\text{cen}}, Z_{\text{cen}})$ of the plasma. Use of an analytically defined coordinate such as θ reduces these other parameter determinations to a sequence of 1-D golden-section searches, each in the radial or ψ-direction.

Since the ITER calculations work directly with (ψ, θ) flux coordinates, it is necessary to calculate the (inverse) mapping functions $R(\psi, \theta)$ and $Z(\psi, \theta)$. Fortunately for limiter calculations, these are only needed at such a distance from the X-point that both are well-behaved functions of ψ. They are calculated point-by-point in much the same way as the other parameters, i.e., for each point (ψ_i, θ_j) of a regular lattice in flux coordinates, a search is conducted along the radius $\theta = \theta_j$ to find (R_i, Z_j) such that $\psi(R_i, Z_j) = \psi_i$. Cubic splines are used throughout to ensure good accuracy, which is tested by combining a forward with a backward mapping, i.e., using (R, Z) evaluated at (ψ_i, θ_j) as argument to $\psi(R, Z)$, and verifying that $|\psi - \psi_i|$ is accurate to at least 1 part in 10^4.

E. Fieldline Tracing

In terms of ψ and $I(\psi)$, the magnetic field components in cylindrical polars are

$$\begin{aligned} B_R &= -\frac{1}{R}\frac{\partial \psi}{\partial Z} \\ B_T &= RI \\ B_Z &= \frac{1}{R}\frac{\partial \psi}{\partial R} \end{aligned} \tag{5}$$

where B_T is the toroidal component of field, directed in the ϕ coordinate. The standard fieldline equation is

$$\dot{\mathbf{x}} = \frac{d\mathbf{x}}{dt} = \mathbf{B}(\mathbf{x}) \tag{6}$$

where dot denotes differentiation with respect to pseudotime t measured along the fieldline. For time-independent fields, it may be helpful to think of t as corresponding to fieldline length. When flux coordinates are used, Eq. (6) simplifies to

$$\frac{d\theta}{d\phi} = RJ(\psi, \theta)/I(\psi) \tag{7}$$

where $J(\psi, \theta)$ is the Jacobian of the mapping transformation.

Although the computational costs of solving the ordinary differential equations of Eq. (6) are usually negligible on modern hardware, it is still important to choose a numerical algorithm tailored to present requirements, namely:

1) relatively inexpensive, because 10^3–10^5 or more fieldlines will need to be computed, corresponding to the size of triangulation of the results geometry;

2) millimeter accuracy in following fieldlines, corresponding to the expected accuracy in the position of PFCs subjected to thermal expansion effects;
3) step sizes such that the fieldline is approximately straight over one step in t, to ensure accurate geometry intersection.

These requirements are most easily met by a low-order scheme with adaptive timestepping to ensure (2). Runge–Kutta–Fehlberg (RKF) also known as (aka) Embedded Runge–Kutta schemes with step adaptation in [17] aka Cash-Karp algorithm are well documented and are relatively easy to implement. There is, however, a further restriction in order of accuracy, for Shampine–Watts relies on a degree of smoothness of the solution $\mathbf{x}(t)$ at least that of the RKF scheme to estimate accurately the error in the integration. As is well known, cubic splines have discontinuous third derivative, hence is sensible to use third-order RKF. Details of the specific schemes implemented are presented in Support Section III.

F. Diagnostics

The diagnostics produced by the SMARDDA codes will be adequately exhibited by plots in Section III and MASTU. Output suitable for the open source plotting tool gnuplot is produced by GEOQ, and all plots of 3-D fields unsurprisingly use the vtk format to be visualized with ParaView [18]. Moreover, ParaView can perform a wide range of analyses of field data, which give it the capability, for example, to calculate the total power deposited on a tile from the contributions of individual elements.

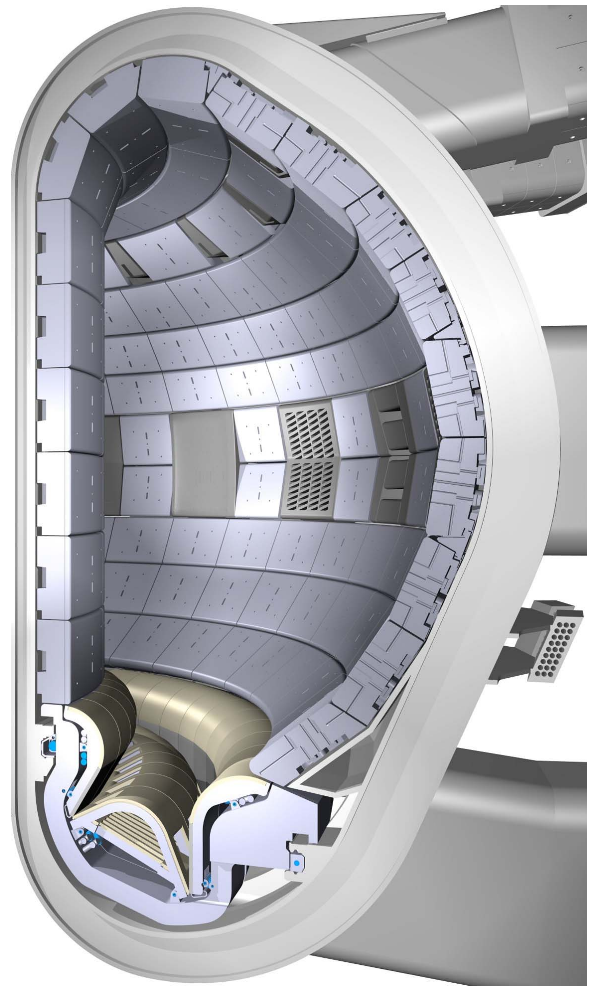

Fig. 4. Vertical cut through detailed ITER model, showing inside the vacuum vessel, in particular the panels covering the side and upper walls.

III. Application to ITER

A. Background

Fig. 4 is produced directly from the ITER CAD database to illustrate the ultimate starting point. CAD descriptions of the panels are extracted, and after defeaturing and repair as explained in Paper I, the restricted surface geometry is triangulated, as described in Section II-C. The resulting meshed geometry is visualized in Fig. 5, where note that each panel appears as two adjacent geometrical blocks (semipanels), since the central strip with the wall fixings has been omitted.

The magnetic field geometry can be understood with reference to Fig. 6. Since the tokamak plasma surface will correspond to a surface of constant flux to good approximation, limiter contact is made on the inside of the torus for this equilibrium. The shadowed panel and the adjacent shadowing panels occupy a volume such as shown in Fig. 6, consequently only the cross-hatched area need be mapped in flux coordinates.

B. Illustrative Results

The results presented are chosen to give a flavor of the effort needed to thoroughly verify and validate SMARDDA for limiter work, as well as demonstrate potentially useful capabilities of the codes. One such is the ability, having calculated fields $\mathbf{B}$ and ψ for each surface, to color each triangle with the value of Q given by Eq. (1). This enables the SMARDDA calculation of Q to be tested against direct evaluation of Eq. (1) using the ParaView calculator, which has its own method for finding $\mathbf{n}$. The resulting Q distribution is calculated at negligible computational cost since no shadowing is performed, but can give insight into surfaces most at risk of overheating (see Fig. 7).

Since the ability to treat CAD is the key, much interest attaches to the influence of the discretization of the geometry on the power deposition results. Fig. 8 is indicative of the results produced on the base mesh, i.e., the mesh produced directly using the CADfix mesher. For the ITER panels, the nominal mesh length is 30 mm, giving 3350 surface triangles on the launch geometry. This translates directly into number of fieldlines followed, of which 382 escape past the shadowing panels and produce the power distribution shown in Fig. 8, for which $P_{\text{loss}} = 7.5$ MW and $\lambda_m = 50$ mm.

In addition to successful comparisons with streamlines produced by ParaView, there was further detailed examination of the fieldline integration algorithm, to understand how control of the local error limits the global error. Thus, it emerged that the fieldlines are so close to being straight in flux coordinates that as few as 10 steps might be needed to get past the shadowing tiles. In any event since here, the relevant computed

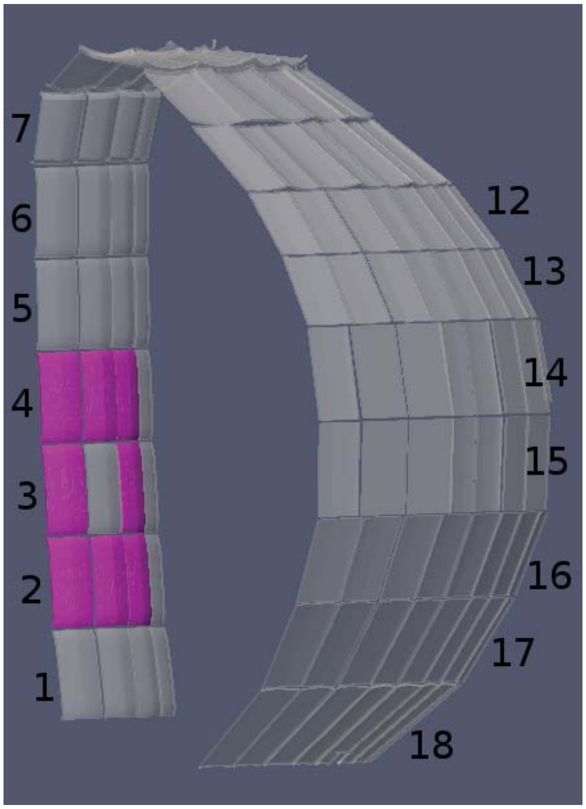

Fig. 5. Surfaces are those of the panels shown in Fig. 4, for a 30° segment of the ITER torus, with its ports blanked off. The numbers refer to horizontal rows of panels. The panels marked in magenta are tested for their ability to shadow the panel they surround.

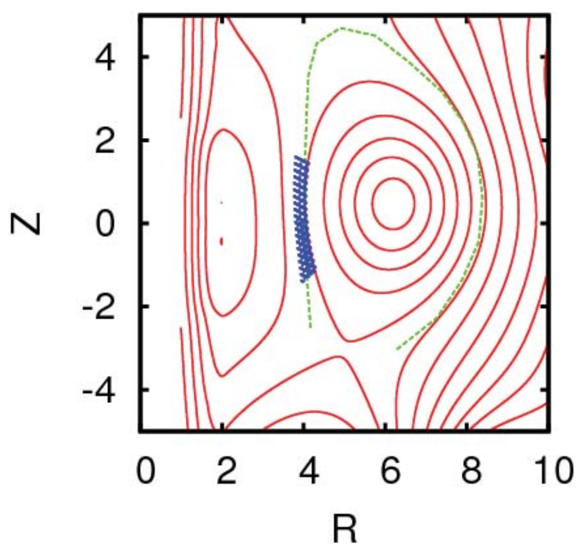

Fig. 6. Contours of magnetic flux ψ for ITER equilibrium with $B_T = 6.0$ T, $I_p = 7.3$ MA. The dashed line corresponds to the inner edge of the first wall in silhouette. The cross-hatching marks the mapped region containing the point where the plasma boundary (LCFS) touches the wall.

properties are the area of shadowing and the Q dependence, the demonstration that changing the integration tolerance ϵ_r makes no appreciable to these properties, suffices to prove acceptable error control. Indeed, Fig. 9 is unchanged if ϵ_r is increased from 10^{-6} to 10^{-4}. Fig. 9 shows the deposition

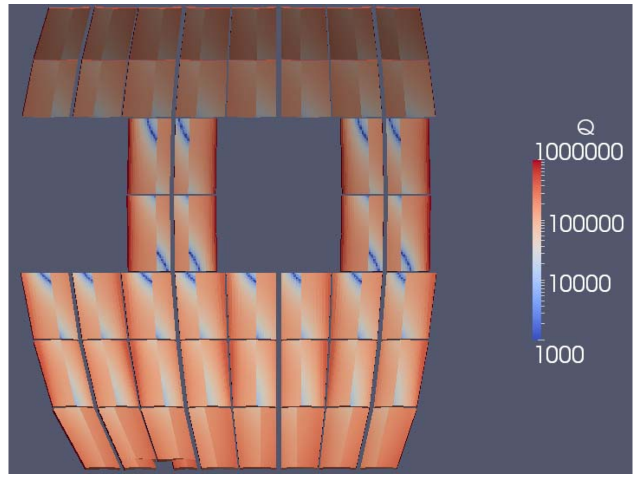

Fig. 7. Outer panels, rows 12 to 18 of the ITER model are shown painted with power Q, ignoring shadowing effects. Equilibrium with $I_p = 7.5$ MA and $B_T = 6.0$ T, $P_{\mathrm{loss}} = 5$ MW, and $\lambda_m = 90$ mm.

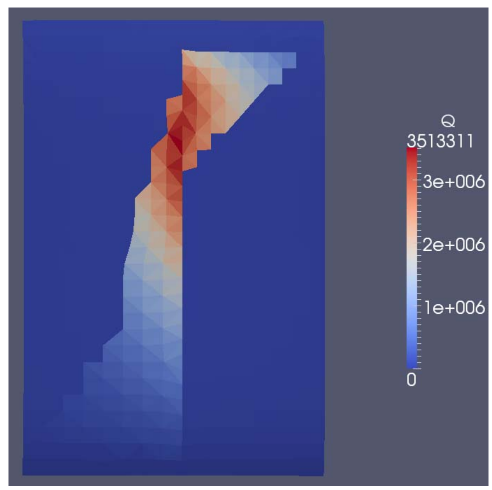

Fig. 8. Power deposited on the central semi-panel accounting for shadowing by its eight nearest neighbors. The base meshing of both results and shadowing geometry has been used.

results for a shadowing geometry refined up to $\times 16$ relative to the base meshing drawn in Fig. 8. As the number of launch points is increased, evidently peak power deposition and Q distribution change little.

The total computation time for most refined calculation was 7 s on an AMD Athlon 64 X2 dual core processor. The tracking calculation took 3.73 s, during which time 53 600 fieldlines were tested for intersection with the 289 040 triangles in shadowing geometry (and 6050 escaped). The approximate time for each fieldline calculation was therefore 70 μs. With approximately 10 steps per fieldline, this gives a cost of 7 μs per straight track, a figure which compares very favorably with similar numbers found Paper I for the duct problem, which had only 2146 triangles. It can be concluded that use of the HDS can make the cost of geometry intersection tests almost independent of geometry complexity.

Lastly, Fig. 10 is an example of a shadowing study used to check the normalization of Q, but also of direct relevance to the designer, for an ITER start-up phase (quasi-)equilibrium

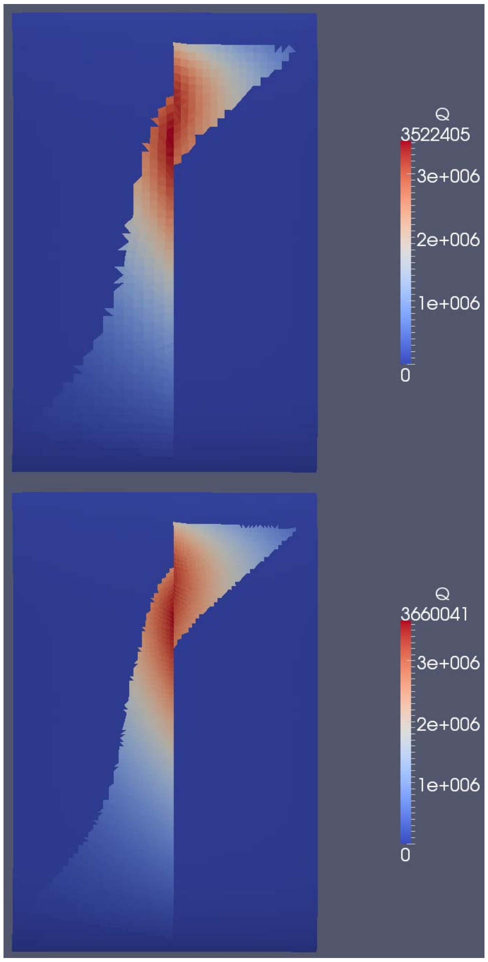

Fig. 9. Power deposited on the central semi-panel accounting for shadowing by its eight nearest neighbors. The base meshing of the results geometry is successively refined ×4 (top) and ×16 (bottom).

at $t = 7.34$ s with $I_p = 3.11$ MA and wall plasma safety factor $q_{\text{wall}} = 8.73$. $P_{\text{loss}} = 3.17$ MW and $\lambda_m = 146$ mm. The line where panel illumination changes from right- to left-handed is where the plasma touches the geometry. Computations were also conducted with 14 panels, which demonstrated that shadowing by second nearest neighbor panels was generally unimportant, except in the case of the ports in rows 14 and 15. These results led onto studies of the effect of small panel misalignments on power deposition, using yet another SMARDDA code VTKTFM to manipulate the vtk files directly to displace and rotate results and shadowing geometries.

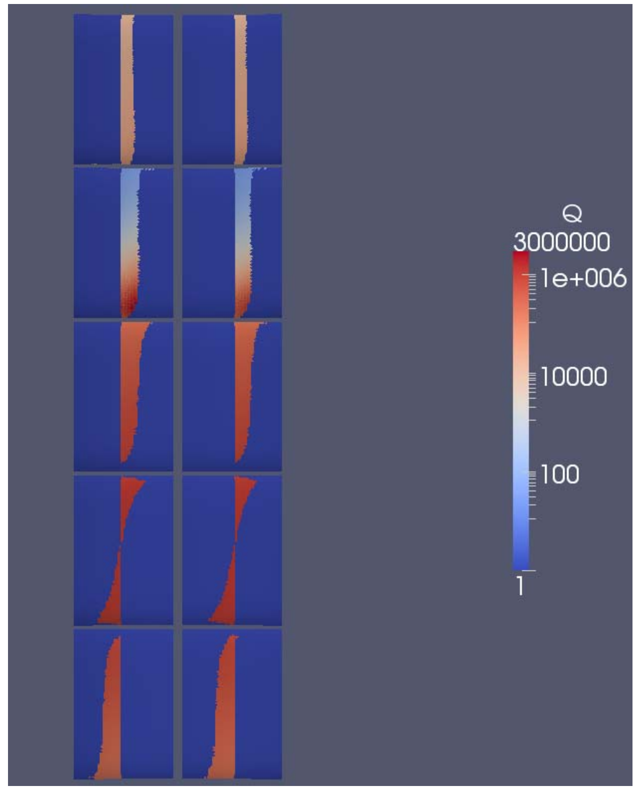

Fig. 10. Power deposited on the panels in rows two to six assuming that each is shadowed by its eight nearest neighbors.

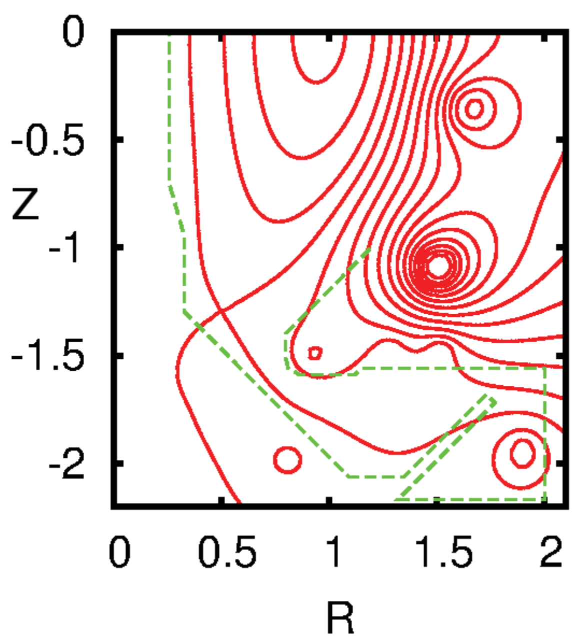

Fig. 11. Contours of magnetic flux ψ for the lower half of MAST-U super-X equilibrium with $B_T = 0.64$ T, $I_p = 1.0$ MA. The dashed line corresponds to the inner edge of the first wall in silhouette.

IV. Application to MAST-U

A. Special Features for MAST-U

The application to divertors is more challenging because the X-point topology means there is no simple 2-D mapping from space to flux-based coordinates, see Fig. 11 near $R = 0.5$ and $Z = -1.3$. Moreover, the fact that the external toroidal confinement field is produced by a set of discrete coils manifests itself as a ripple with period in the toroidal direction proportional to $1/N_s$, where the number of coils $N_s = 12$ for MAST (see Fig. 12). Tokamak TF coils are generally designed so that this ripple is negligible in the central plasma region, but the ripple requires special treatment in MAST-U, because existing physical constraints virtually force the divertor into a space near the TF conductors, see Section IV-A.1. However, since twelvefold symmetry extends to the divertor geometry it is sufficient to work with a 30° segment, see Section IV-A.2.

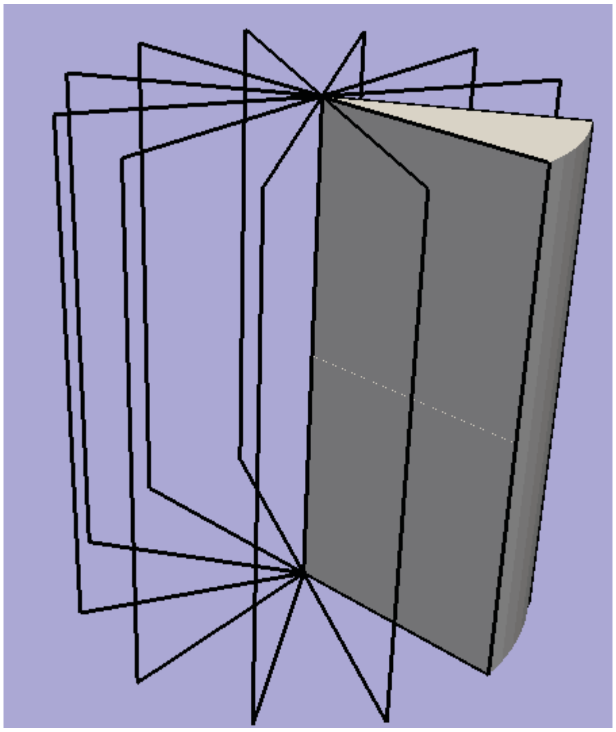

Fig. 12. Sketch of MAST TF coils, shown as black lines, with current feeds omitted for clarity. Only the geometry in the lower half of a 30° segment (marked) need to be modeled.

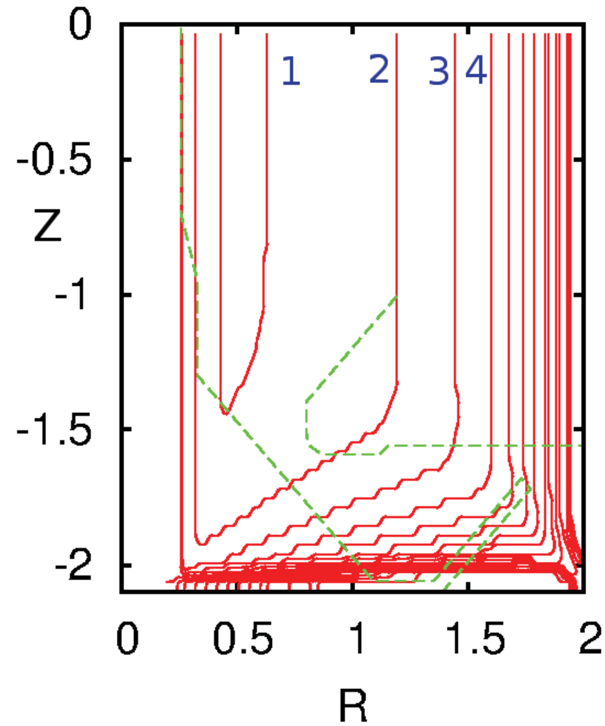

Fig. 13. Contours of $N_{m\zeta}$ needed to reproduce field component $B_{\zeta v}$ to a given accuracy $\epsilon_m = 10^{-6}$ as a function of (R, Z). The four lowest contours are labeled with their $N_{m\zeta}$ values.

1) Ripple Field: The treatment of the ripple requires provision of all the three components of the magnetic field generated by a set of current loops such as sketched in Fig. 12. Indeed, preliminary power deposition calculations were performed using the magnetic field from exactly this current configuration. However, detailed investigations, which will be reported elsewhere, revealed that it was important to account both for the finite width of the conductors and for the current feeds. In either case, the magnetic field is provided to SMARDDA as sample values on a uniform grid in (R, ϕ, Z) coordinates covering the volume sketched in Fig. 12. (The distinction between the use of ϕ and ζ for angular coordinate in the toroidal direction is explained in Support Section II).

As in Section III, **B** component values at an arbitrary point (R, Z) are calculated by direct product cubic spline interpolation between the supplied mesh values. However, for interpolation in toroidal angle ζ, the periodicity makes optimal the use of a Fourier series representation. The actual coil geometry lacks reflectional symmetry so the vacuum magnetic field dependence on ζ has to be written

$$B_{iv} = B_{i0} + \Sigma_{m=1}^{m=N_m} B_{ism} \sin m\xi + \Sigma_{m=1}^{m=N_m} B_{icm} \cos m\xi \quad (8)$$
$$i = R, \quad Z, \quad \zeta$$

where N_m is determined by the data sampling rate, and the scaled angle $\xi = N_s \zeta$. Since 32 samples in ξ are provided, $N_m = 16$ provides an exact representation of the data at uniformly spaced intervals in ξ or ζ.

The Fourier expansion coefficients B_{icm} and B_{ism} in Eq. (8) are straightforwardly evaluated using fast Fourier transforms, and the mode spatial dependences examined. At each (R, Z), the minimum number of angular modes N_{mi} necessary to reproduce the samples of field component B_{iv} to a specified relative tolerance ϵ_m may be computed, and contour plots such as Fig. 13 are be produced. The field design ensures that the hottest plasma occupies a region where the field is close to axisymmetric, so that $N_{m\zeta} \geq 2$ is required only for the extremities of the divertor region. The local axisymmetry also makes it easy to normalize $\mathbf{B}_v$ consistent with I used in the magnetic equilibrium calculation.

Accounting for ripple, the fieldline integration Eq. (6) becomes, since the fieldlines are unchanged when each component is multiplied by an identical function of position

$$\begin{aligned} \dot{R} &= -\frac{\partial \psi}{\partial Z} + R B_{Rv} \\ \dot{Z} &= \frac{\partial \psi}{\partial R} + R B_{Zv} \\ \dot{\xi} &= N_s B_{\zeta v} \end{aligned} \quad (9)$$

and is solved in the natural coordinates (R, Z, ξ). To solve (9), it was found computationally efficient to selectively mask out the higher mode numbers of the vacuum field $\mathbf{B}_v$ depending on the position. Using a relative tolerance of $\epsilon_m = 10^{-6}$ to determine the mask, the cost of following fieldlines in the divertor region could be reduced by a factor of two. Further economy was achieved by tracing fieldlines only as far as the plane $Z = -1.29$ m below the center of MAST,

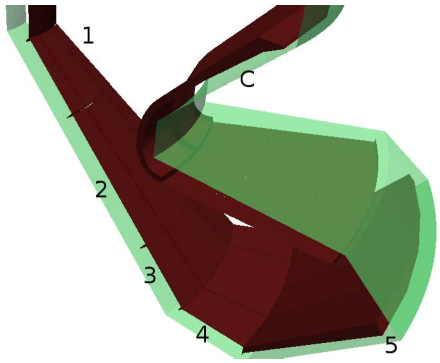

Fig. 14. Dark surfaces are those of the geometry modeled for a 30° segment of a MAST-U divertor design. An enveloping bean-can to catch any leakage of fieldlines through the tiles is shown as a lighter halo. The numbers refer to horizontal rows of tiles in the divertor and C labels the coil armor shadowing geometry.

where it is certain that they are able to connect power from the midplane.

As in Section III-B, both analysis and single fieldline numerical calculation were used to establish conservative parameter values for fieldline tracing of sufficient, millimeter accuracy. In particular, it was found preferable to use an absolute tolerance ϵ_a for fieldline integration. This tolerance was then used to calculate power deposition profiles, which were found to be invariant under order of magnitude increases in ϵ_a, for example.

2) Symmetry: Fig. 14 shows a representative one-twelfth of the MAST-U geometry in and above the divertor, indicating the locations of tiles T1–T5. Testing for fieldline intersections with the complete 360° device is achievable using this 30° sector, by applying the periodic condition $\mathbf{x}(R, Z, \xi + 2\pi) = \mathbf{x}(R, Z, \xi)$ when fieldlines exit the sector.

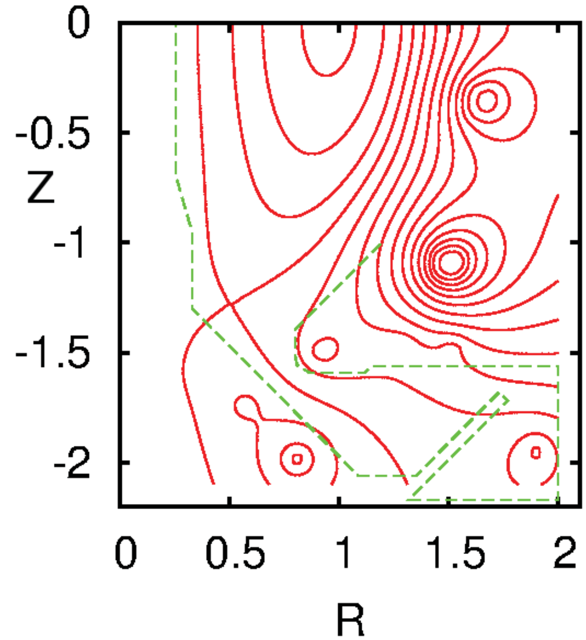

Fig. 15. Contours of magnetic flux ψ for a MAST-U intermediate equilibrium.

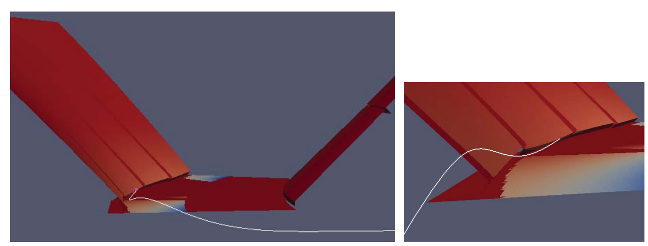

Fig. 16. MAST-U intermediate equilibrium. The plots of views from two slightly different directions show how a fieldline (in white) may get into the T4/T5 gap in one design.

B. Illustrative Results

The MAST-U calculations represent the most demanding application of SMARDDA to date since the fieldlines may be long in terms of both number of circuits around the vertical axis and the number of steps often exceeds 500 (average 100). Furthermore, although the geometry is physically smaller, it contains as much detail, as in Section III. An important design goal of MAST-U is the ability to handle the super-X field configuration [3] as well as the usual X-point arrangement, which in practice means the ability to handle intermediate configurations wherein power can be deposited on any of tiles T1–T5. All equilibria have $B_T = 0.64$ T and $I_p = 1.0$ MA, with additional shaping by varying the current in external poloidal field coils, the location of which can be deduced from the extrema of ψ in Fig. 11.

Detailed realistic predictions of power deposition are of interest principally to MAST-U designers. With ease of exposition in mind, scrape-off layer width is taken as $\lambda_m = 10$ mm, rather than the more realistic 3 mm to make the plots of power deposition easier to visualize. The total power loss is set to be $P_{\text{loss}} = 1$ MW, a quantity chosen on the grounds that it is easily scalable to other values, but it is not actually a physically expected value. In this context of easier exposition, deployment of SMARDDA to examine the uniformity of power deposition will be described in Section IV-B.2, and use of the software to identify issues raised by preliminary examination is documented in Section IV-B.1, immediately below.

1) Identification of Issues: The equilibrium of Fig. 15 shows that the plasma scrape-off layer, approximated by the contour passing through the X-point, is located close to the boundary between the tiles T4 and T5. Plots of Q deposition showed that there was power deposited on the lower edge of T5, at potentially significant levels because of near-normal fieldline incidence. This would be unexpected in an axisymmetric field, but Fig. 16 shows that the field ripple is sufficiently large at the T4/T5 gap to allow it. Further examination verified that the total power deposited on the edge of one T5 tile was less 0.1% of the total loss, i.e., negligible.

Calculations of power deposited by a standard X-point plasma on tiles T2 and T3 showed a similar failure of shadowing. This issue was resolved by making minor modifications to the design.

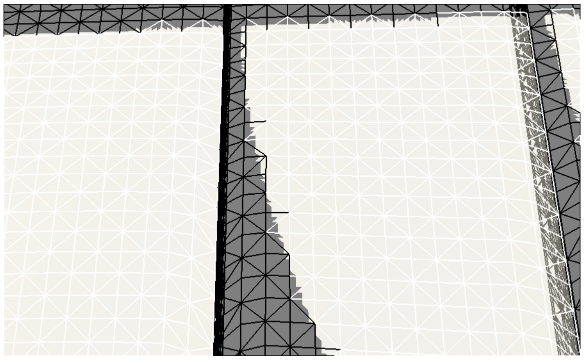

Fig. 17. Power deposition shadows for super-X equilibrium. Expanded view of the upper region of T5 surfaces showing a superposition of illuminated areas from calculations with a coarse mesh and the same mesh with 16× refinement. The coarse mesh illumination is marked by the edges of the mesh triangles (black for shadow) whereas the finer mesh illumination is indicated by solid white.

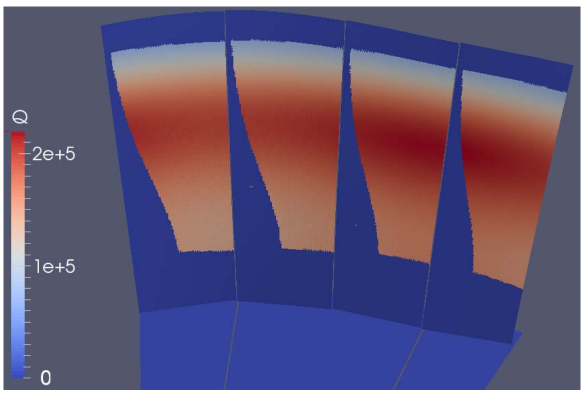

Fig. 18. Distribution of power deposited on T5 tiles for a MAST-U super-X equilibrium, with revised tile design, $\lambda_m = 10$ mm.

2) Distribution of Power Deposition: Observe from Fig. 17 that overlaying the Q distributions for different meshings of the geometry shows changes only in Q at the cutoff boundaries, which clearly correspond to the triangle subdivision algorithm. Once this has been verified and the fieldline tests mentioned in Section IV-A.1 has been passed, detailed calculations may be performed to demonstrate uniformity of power deposition on tiles as the equilibrium properties are varied.

Fig. 18 is indicative of the results obtained. The variation in total power deposited varies from tile to tile by under 5%. The total computation time for this calculation was just over an hour, viz., 4000 s spent testing 67 776 fieldlines for intersection with the 29 063 triangles in the shadowing geometry from which about half of the fieldlines escape. The approximate time for each fieldline calculation was therefore 60 ms. The three orders of magnitude increase in cost relative to the ITER calculations is accounted for by much longer fieldlines' forming a higher percentage of the total, and the large increase in the number of calculations needed to evaluate **B**.

Lastly, Fig. 19 shows how the Eich formula gives finite power deposition within the private flux region, for tiles T1 and T2. As in the case of the simpler formula, the power

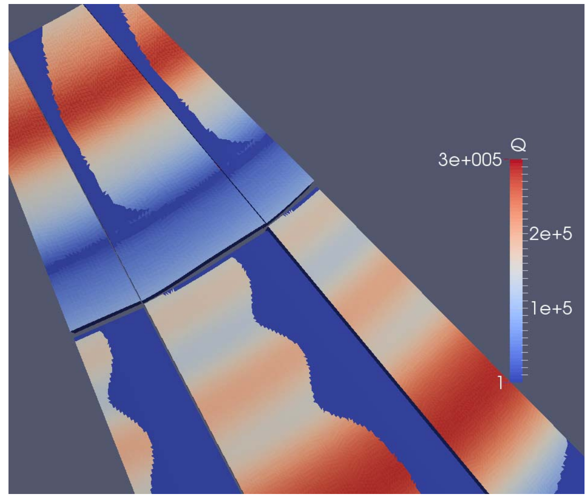

Fig. 19. Distribution of power deposited on tiles T1 and T2 for a MAST-U X-point equilibrium using the Eich formula with overlarge $\sigma = \lambda_q = 10$ mm. The immediate neighborhood of the horizontal band without power on (the upper tile) T1 is an artifact.

fall-off lengths have been deliberately exaggerated for ease of exposition, which here has the useful side effect of maximizing the area of illumination, thereby exposing any areas where power is deposited anomalously.

ACKNOWLEDGMENT

The authors would like to thank R. Mitteau of ITER, G. Saibene of F4E, and P. J. Lomas of CCFE for their valuable input and discussions. Magnetic equilibrium fields for ITER and MAST-U, respectively, were calculated and supplied by M. Mattei of Consorzio CREATE, Second University of Naples, and G. Cunningham of CCFE. D. Taylor of CCFE helped with the MAST ripple field. CAD files for ITER and MAST-U geometry, respectively, were supplied by G. Saibene of F4E and N. Richardson of CCFE.

To obtain further information on the data and models underlying this paper please contact PublicationsManager@ccfe.ac.uk. The views and opinions expressed herein do not necessarily reflect those of the European Commission.

REFERENCES

[1] W. Arter, E. Surrey, and D. B. King, "The SMARDDA approach to ray-tracing and particle tracking," *IEEE Trans. Plasma Sci.*, submitted, preprint arXiv 1403.6750.

[2] R. Aymar, P. Barabaschi, and Y. Shimomura, "The ITER design," *Plasma Phys. Controlled Fusion*, vol. 44, no. 5, pp. 519–565, 2002.

[3] I. Katramados *et al.*, "MAST upgrade closed pumped divertor design and analysis," *Fusion Eng. Des.*, vol. 86, no. 9, pp. 1595–1598, 2011.

[4] R. T. McGrath, "Shaping of the plasma facing surfaces of the ALT-II full toroidal belt limiter," *Fusion Eng. Des.*, vol. 13, no. 3, pp. 267–282, Dec. 1990.

[5] [Online]. Available: http://www.vtk.org

[6] A. Henderson, *ParaView Guide, A Parallel Visualization Application*. New York, NY, USA: Kitware, 2007.

[7] R. Mitteau, A. Moal, J. Schlosser, and D. Guilhem, "Heat flux deposition on plasma-facing components using a convective model with ripple and Shafranov shift," *J. Nucl. Mater.*, vol. 266, pp. 798–803, Mar. 1999.

[8] J. Velasco, A. Bustos, F. Castejón, L. Fernández, V. Martin-Mayor, and A. Tarancón, "ISDEP: Integrator of stochastic differential equations for plasmas," *Comput. Phys. Commun.*, vol. 183, no. 9, pp. 1877–1883, 2012.

[9] F. Maviglia *et al.*, "Electromagnetic models of plasma breakdown in the JET tokamak," *IEEE Trans. Magn.*, vol. 50, no. 2, pp. 937–940, 2014.

[10] A. Glasser, "The direct criterion of newcomb (DCON) for the stability of an axisymmetric toroidal plasma," Los Alamos Nat. Lab., Los Alamos, NM, USA, Tech. Rep. LA-UR-95-528, 1997.

[11] R. J. Goldston, "Heuristic drift-based model of the power scrape-off width in low-gas-puff H-mode tokamaks," *Nucl. Fusion*, vol. 52, no. 1, p. 013009, 2012.

[12] A. Loarte *et al.*, "Chapter 4: Power and particle control," *Nucl. Fusion*, vol. 47, no. 6, p. S203, 2007.

[13] T. Eich, B. Sieglin, A. Scarabosio, W. Fundamenski, R. Goldston, and A. Herrmann, "Inter-ELM power decay length for JET and ASDEX upgrade: Measurement and comparison with heuristic drift-based model," *Phys. Rev. Lett.*, vol. 107, no. 21, p. 215001, Nov. 2011.

[14] R. Albanese, G. Calabrò, M. Mattei, and F. Villone, "Plasma response models for current, shape and position control in JET," *Fusion Eng. Des.*, vols. 66–68, pp. 715–718, Sep. 2003.

[15] G. Cunningham, private communication, 2012.

[16] C. de Boor, *A Practical Guide to Splines*. New York, NY, USA: Springer-Verlag, 1978.

[17] L. F. Shampine and H. A. Watts, "The art of writing a Runge–Kutta code. II.," *Appl. Math. Comput.*, vol. 5, no. 2, pp. 93–121, Mar. 1979.

[18] W. Schroeder, K. Martin, and B. Lorensen, *The Visualization Toolkit. An Object-Oriented Approach To 3D Graphics*. New York, NY, USA: Kitware, 2006.

Wayne Arter (M'98) received the M.A., M.Math., and Ph.D. degrees from the University of Cambridge, Cambridge, U.K.

He has been involved in computational physics at Culham, U.K., since 1982, apart from a sabbatical year teaching numerical analysis at the University of Arizona, Tucson, AZ, USA, and a year involved in software projects for Vector Fields Ltd., Oxford, U.K. Most of his career has been with the United Kingdom Atomic Energy Authority, except for 10 years spent in the private sector from 1996 to 2006. His private sector research included computational electromagnetics, in particular, the modeling and design of microwave sources, and the development of the INSTANT ray-tracing code for BAE Systems. His current research interests include providing technical input to a wide range of projects, from tokamak plasma physics modeling to neutron shielding, and activation problems.

Valeria Riccardo, photograph and biography not available at the time of publication.

Geoff Fishpool, photograph and biography not available at the time of publication.